communications earth & environment

Article

A Nature Portfolio journal

https://doi.org/10.1038/s43247-025-02196-2

Climate driven generative time-varying model for improved decadal storm power predictions in the Mediterranean

Nazzareno Diodato [1], Cristina Di Salvo [2] & Gianni Bellocchi [1,3]

Decadal climate predictions are crucial for communities engaged in scenario planning under Sustainable Development Goals. However, uncertainties in future precipitation extremes hinder climate mitigation and adaptation efforts. Here we present a hybrid statistical climate-driven time-varying model to predict the Areal MEan Storm Erosivity Index, a key indicator of hydrological events, for the Mediterranean region. By integrating historical data (1884-2022) with large-scale (El Niño–Southern Oscillation) and small-scale (precipitation variability) climate forcings, our model captures past storm behavior and projects future dynamics. The Hurst exponent (0.63) suggests a long-term positive memory in Areal MEan Storm Erosivity Index, enhancing prediction accuracy. Projections show an Index increase until 2040, then a decline until 2050, and a resurgence. While consistent with other regional models at the interdecadal scale, finer variations are less pronounced at the interannual scale. This approach offers valuable insights into hydroclimate variability, aiding climate resilience planning in the Mediterranean and beyond.

Decadal timescales have emerged as vital planning horizons for governments, businesses and society, offering an attractive tool for short-term climate change adaptation and mitigation planning[1,2]. Despite this recognition, relevant gaps persist in our understanding and prediction of precipitation patterns, particularly at regional scales, representing notable deficiencies in climate science[3,4]. Extreme rainfall events, in particular, pose relevant threats, regarded as one of the most damaging climate hazards[5], raising concerns about their changing frequency and intensity[6]. In this context, advancing the central role of extreme weather events prediction and information, which is closely embedded in climate dynamics[7], is a critical contribution to achieving the Sustainable Development Goals[8].

Storm-power indicators effectively support climate prediction and guide landscape conservation planning efforts[9]. Moreover, historical and statistical climatology plays a crucial role in understanding how the Earth system responds to such climate forcing mechanisms. Rainfall erosivity is pivotal in informing the development of conservation and environmental management plans in a changing climate[10]. By assessing the power of rainfall through kinetic energy evaluation and associated runoff rates[11], rainfall erosivity serves as a reliable indicator of potentially damaging hydrological events[12–14]. Its utility extends beyond immediate applications, aiding in understanding surface-process dynamics, including erosional soil degradation, flash floods and landslides. As such, it provides an opportunity to detect the fingerprint of recent climate change[15].

The incorporation of rainfall erosivity into climate change studies has been increasing[16,17] due to its interconnection with the global water cycle, amplifying rainfall erosivity pathways[18] and impacting damaging hydrological events (Fig. 1).

This relationship is particularly pertinent in regions like the Mediterranean, characterised by complex atmospheric and landscape dynamics, making it a hotspot for climate change research[19,20]. The vulnerability of the Mediterranean region to extreme weather events highlights the urgency in studying weather extremes here and improving climate and precipitation forecasting[21,22], with a specific focus on storm development[23] and rainfall erosivity patterns[17].

Despite the wealth of observational record data and climate model simulations[24], uncertainties in future climate persist[25]. Incorporating convection-permitting simulation processes for storm erosivity prediction, advanced physical models face computational constraints[26] and uncertainties associated with model selection[27]. For instance, limitations in these models can lead to overestimation of precipitation in mountainous regions and underestimation of sub-daily extreme rainfall over flat terrain in the central Mediterranean[28]. These challenges highlight the need for com-

[1]Met European Research Observatory – International Affiliates Program of the University Corporation for Atmospheric Research, 82100 Benevento, Italy. [2]Institute of Environmental Geology and Geoengineering, National Research Council, Area della Ricerca di Roma 1, Via Salaria Km 29.300, C.P. 10, 00015 Monterotondo Stazione, Rome, Italy. [3]Université Clermont Auvergne, INRAE, VetAgro Sup, UREP, 63000 Clermont-Ferrand, France. e-mail: gianni.bellocchi@inrae.fr

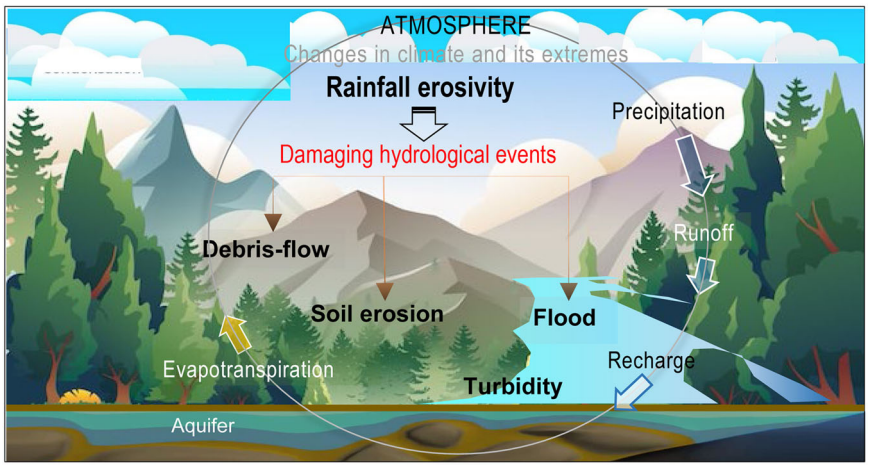

Fig. 1 | Conceptual representation of how climate can influence rainfall erosivity and leading damaging hydrological events through the water cycle. Vegetation cover modulates the water cycle, affecting precipitation patterns and rainfall erosivity. Summer and autumn rainstorms magnify soil erosion, slope destabilisation, and agriculture impacts compared to winter. Enhanced rainfall erosivity increases sediment yield, leading to higher turbidity in water bodies, which degrades water quality and amplifies the consequences of hydrological events. Background image source: Freepick (https://www.freepik.com/free-vector/gradient-mountain-landscape_20547362.htm#query=landscapes&position=27&from_view=search&track=sph&uuid=c02f4319−4d24−4b00-b14a-6ecfa2cf5dbc).

plementary research using data-driven statistical models (DDSMs). DDSMs offer simpler yet effective approaches to understanding past climate variability and its implications for future climate outcomes, presenting viable alternatives to complex dynamical climate models[1,29]. However, decadal prediction remains a major challenge[30–34], necessitating innovative strategies to address forecasting operations and effective communication[35]. In this respect, DDSMs represent a promising strategy as they are trained with an autoregressive pattern that incorporates memory from training time-series, allowing the model to use internal natural variability as a crucial source of information with potential implications for future climate outcomes. Recent years have seen the emergence of various data-driven techniques to uncover correlations between past climate variability and future predictions[36]. Notably, Autoregressive Integrated Moving Average (ARIMA) models have shown effectiveness in predicting precipitation[37,38]. However, the prediction of extreme variables remains uncommon in modern autoregressive models[34,39]. To assess the persistence of these changes in the future, we introduce the Areal MEan Storm Erosivity Index (AMESEI), integrated into a DDSM framework.

AMESEI provides a suitable strategy for addressing the multi-scale challenges of hydrological damaging events at the decadal prediction scale across the Mediterranean region. Our approach offers an innovative solution to the limitations of conventional rainfall erosivity metrics[16], especially when dealing with large-scale, long time-series data. One of the most intriguing aspects of applying DDSMs to climate prediction is their ability to incorporate input at different time scales in the prediction information flow. Precipitation is a notable example. DDSMs can be characterised over certain time ranges by scaling relationships in the form of autoregressive distributions and autocorrelation functions in conjunction with exogenous input. As a reliable indicator of both rainfall erosivity and damaging hydrological events (DHEs), AMESEI requires sophisticated forecasting methods to account for its inherent non-stationarity and seasonal variability. To this end, we have adopted a periodic time-varying autoregressive moving average with conditional standard deviation (PARMAX(TVAR)-CSD) model, an advanced hybrid statistical approach. This model combines periodic autoregressive (PAR) capabilities with exogenous inputs, time-varying coefficients and conditional heteroscedasticity to address the complex dynamics of AMESEI. Specifically, the PARMAX component captures periodic variations while incorporating external variables – here, a Climate Driving Index - that significantly influence the dynamics of AMESEI. The TVAR aspect enables the model to dynamically adjust parameters over time, accommodating non-stationary processes. Meanwhile, the CSD component enhances robustness by addressing variability to changes (volatility) in conditional standard deviations, especially under extreme hydrological events. This model was chosen over simpler alternatives, such as stationary autoregressive models or those lacking exogenous inputs, due to its ability to effectively capture AMESEI's complex, seasonally dependent behaviour and interactions with external climate drivers. By incorporating exogenous predictors and time-varying parameters, the PARMAX(TVAR)-CSD model provides more accurate forecasts and mitigates nonlinearity in the input-output relationships. Furthermore, innovative scaling methods have been employed to analyse AMESEI evolution and variability over multi-decadal periods, leveraging climate data to reduce uncertainties in forecast outcomes. The inclusion of time-varying (TVAR) parameters provides an important advantage by enabling real-time monitoring of frequency shifts, thus allowing for the selection of the most reliable forecasts among chaotic temporal variations[40]. At the same time, exogenous components minimise the model's reliance on autoregressive-only dynamics, further improving its predictive accuracy and stability[41].

In this study, our focus lies on the Mediterranean region, a 7,845,000 km^2 geographical area that remains largely unexplored despite indications from historical data of a rising trend in storm rainfall and erosive precipitation[15], a pattern that echoes similar trends observed in other parts of Europe since the 1960 s[42]. The annual rainfall erosivity over the Mediterranean region ranges from a minimum of 100 MJ mm ha^{-1} h^{-1} yr^{-1} (Tabriz, Iran) to a maximum of 3213 MJ mm ha^{-1} h^{-1} yr^{-1} (Montevergine, South-Italy), with most of the sites having values of 700-1400 MJ mm ha^{-1} h^{-1} yr^{-1} [43] and an estimated average >1000 MJ mm ha^{-1} h-1 yr^{-1}; this corresponds to about a half of the estimated global mean rainfall erosivity (2,190 MJ mm ha^{-1} h^{-1} yr^{-1}, Panagos et al.[11]). Located in the southern part of the European continent (Fig. 2a, white squared), the Mediterranean region exhibits complex interactions between atmospheric and landscape systems, owing to dominant landform features such as sea, land and orography[44].

This complexity gives rise to geographical and temporal variability in the distribution of rain-generating erosivity episodes. Synoptic circulation patterns play a pivotal role in shaping the annual and seasonal distribution of precipitation in the Mediterranean. These patterns advect a mixture of air masses from different regions, including the Atlantic, polar maritime and subtropical regions, and give rise to different degrees of rainfall erosivity (Fig. 2b). The AMESEI pattern (Fig. 2c) exerts its influence on three main areas of the Mediterranean region: the western part of the Iberian Peninsula, Italy, and the Balkans and western Greece. Notably, seasonal variability is pronounced (Fig. 2d), with 34% of storm erosivity occurring between September and November, coinciding with a stronger correlation with hydrological extremes. This period is particularly conducive to surface water floods and flash-flood events, which are more prevalent during this period (Fig. 2d, right axis).

The primary objective of the modelling technique employed in this study is to minimise uncertainty in the interannual variability by considering both large-scale influences, such as the El Niño-Southern Oscillation (ENSO) teleconnection, and smaller-scale climatic forcing represented by the variation coefficient of extreme rainfall. Designed for the Mediterranean region, the PARMAX(TVAR)-CSD model was

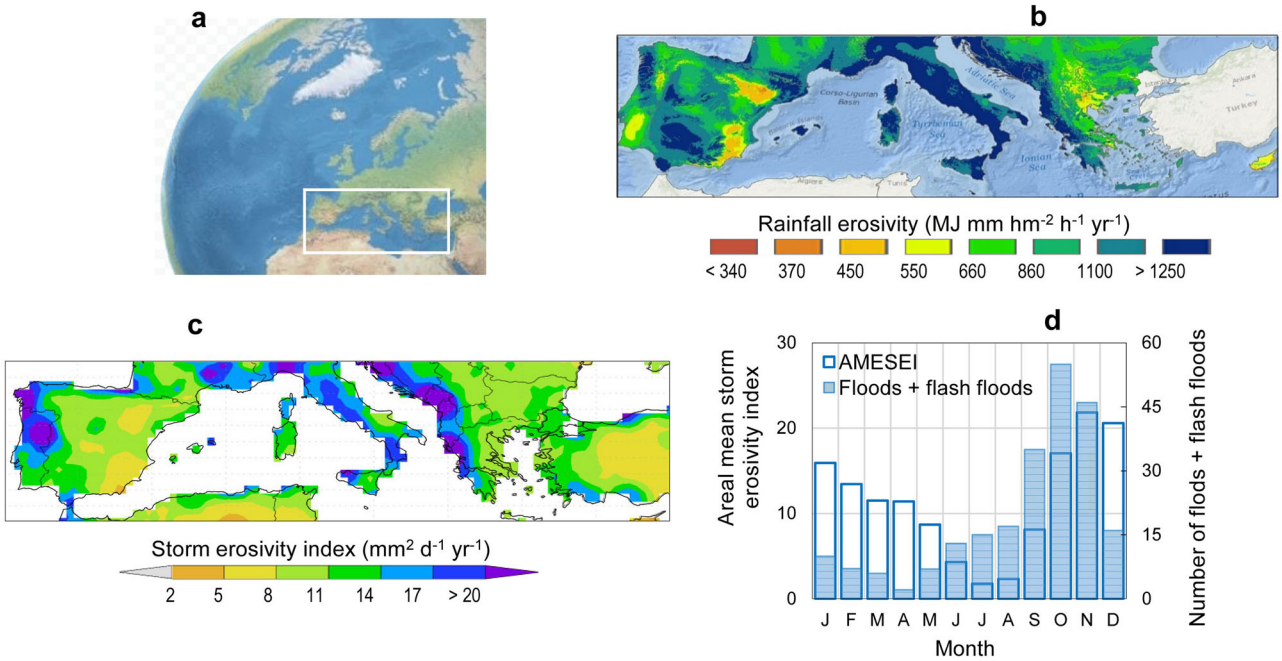

Fig. 2 | Environmental setting, rainfall erosivity and hydrological extremes in the Mediterranean region. a Map of the Mediterranean region (white square, source: Shaded Relief, http://www.shadedrelief.com/natural2/globes.html); (**b**). Annual mean rainfall erosivity averaged over the period 2002−2012 (data sources: Climate Explorer, http://climexp.knmi.nl; GLDAS, [47]); (**c**) Annual mean rainfall erosivity averaged over the period 2002−2012 (data source: Rainfall Erosivity Database on the European Scale REDES[99]). **d** Monthly AMESEI (empty histogram, 1970–1916), and sum of floods and flash-floods (blue histogram, 1940−2015) for the Mediterranean region (data source[100]).

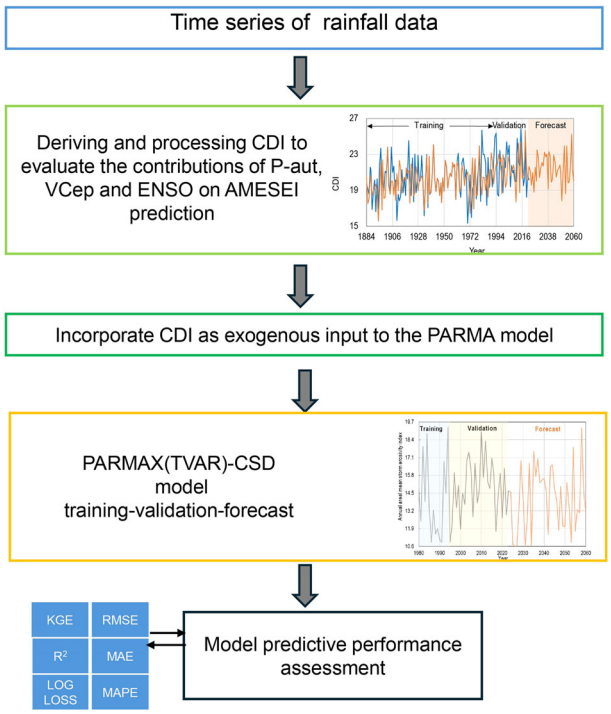

Fig. 3 | Workflow for the PARMAX(TVAR)-CSD model. The workflow shows how the model was used to predict AMESEI in the Mediterranean region.

trained using data from 1884 to 1992, and validated over the period 1993–2022. The PARMAX(TVAR)-CSD workflow, including the steps leading to its application to project climate conditions for the period 2023–2060, is illustrated in Fig. 3.

Results and discussion

Incorporating exogenous climate variables in decadal prediction models

Studies have demonstrated the efficacy of integrating decadal predictions into DDSMs due to the additional predictability provided by long-term climate oscillation signals[45]. This is supported by previous studies[46], in which it was found that forecasts incorporating teleconnection patterns exhibited improved predictive ability for several years ahead compared to those without forcing[46]. These studies, including the present one, highlight the combined influence of internal climatic variability and external forcing (e.g., precipitation amount, variability of extreme hydrological events and ENSO) on decadal projections. Figure 4a illustrates the relationship between the AMESEI and two key precipitation metrics: the variation coefficient of extreme precipitation (VCep) and autumn precipitation amount (P_{aut}). The VCep is a statistical measure that represents the relative variability of extreme precipitation events, calculated as the ratio of the standard deviation to the mean of extreme precipitation intensities over a given period. This metric highlights regions and timeframes where precipitation extremes exhibit relevant fluctuations, offering insights into the potential for erosive events. VCep is commonly used to quantify precipitation variability in climate studies (e.g.[47]). Throughout the Mediterranean region, VCep is positively correlated with AMESEI, with Pearson's correlation coefficients (r) exceeding 0.5 in most areas and reaching values above 0.8 in some locations. These findings align with previous studies, such as[48], which show that storm variability contributes to rainfall erosivity and sediment production. In contrast, Fig. 4b reveals a weaker relationship between autumn precipitation (P_{aut}) and AMESEI, with correlation coefficients around 0.3, although values near 0.5 are observed in the Iberian Peninsula and Balkans. We acknowledge that Pearson's correlations may miss complex, non-linear interactions. While future studies could explore mutual information to reveal deeper nuances in the data[49,50], this study prioritised linear correlations to establish clear, quantifiable relationships for guiding model development. To further assess the combined influence of precipitation amount,

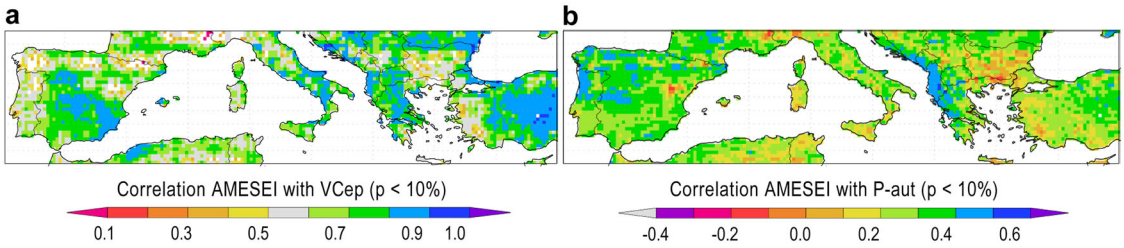

Fig. 4 | Influence of precipitation characteristics on the Areal Mean Storm Erosivity Index (AMESEI). a Correlation between AMESEI and the variation coefficient of extreme precipitation (VCep) during the 1970−2016 period. Data sources: Global Land Data Assimilation System (GLDAS, 0.25° resolution. https://ldas.gsfc.nasa.gov/gldas; [47]) and SDII-and Rx1day(s-aut). **b** Correlation between AMESEI and autumn precipitation amount (P_{aut}) during the 1970−2016 period. Data source: E-OBS gridded dataset (0.25° resolution; https://www.ecad.eu/download/ensembles/download.php; Cornes et al. [76]). Climate Explorer (http://climexp.knmi.nl) was used for map generation and updates.

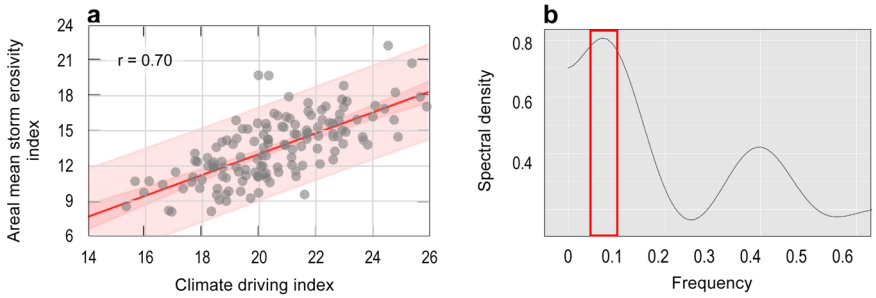

Fig. 5 | Modelling Mediterranean Areal Mean Storm Erosivity Index (AMESEI). a Scatterplot of the relationship between the model's exogenous input (Climate Driving Index) and AMESEI values from 1884 –2022. The inner (deep pink) and outer (light pink) areas indicate the 90% and 95% confidence intervals, respectively; (**b**) Spectral density plot of the distribution of frequencies in the Mediterranean AMESEI time-series The red box indicates the most likely frequency range for the PARMAX(TVAR)-CSD model cycle.

variability of extreme hydrological events (as captured by *VCep*), and ENSO on decadal predictions, we used the Climate Driving Index (*CDI*) as exogenous data.

The *CDI* serves as a key indicator of climate variability in the central Mediterranean region, incorporating both small–scale (autumn precipitation amount and variability of hydrological extremes) and large–scale (Niño3.4) climate-driven factors. Previous research on the Mediterranean region has shown that the variation coefficient of extreme precipitation (VCpe) and the storm erosivity index can be influenced by changes in short-term rainfall properties, shifts in seasonal distribution patterns of rainfall and year-to-year variability in precipitation[51]. Additionally, studies like[52] have found El Niño years tend to see increased heavy rainfall, particularly across the central Mediterranean. This finding aligns with the combined effects captured by the *CDI*.

Our model incorporates various factors through the exogenous input ($X \cdot \beta_L$) defined in Eq. 3, where X = *CDI*. The *CDI*, Eq. 5 is a composite metric combining key climatic and hydrological variables - ENSO(3.4), autumn precipitation (P_{aut}), and the variation coefficient of extreme precipitation (VCep)—as detailed in the Data and Methods section. This index encapsulates the combined influence of these drivers on AMESEI, enhancing the model's capacity to capture external forcing mechanisms. Figure 5a illustrates the linear relationship between the *CDI*, Eq. 5 and AMESEI. Notably, most data points reside within the 95% prediction boundaries, with only a few outliers (four points). This observation suggests a statistically significant relationship between AMESEI and the *CDI*, supported by a *p*-value < 0.001 in the ANOVA test. Additionally, the Durbin-Watson test[53,54] was used to check for autocorrelation in the residuals. The Durbin-Watson statistic can range between 0 and 4, a value of 2.0 indicates no autocorrelation in the sample. Values from 0 to < 2 suggest positive autocorrelation, while values from 2–4 suggest negative autocorrelation. In our case, the Durbin-Watson statistic is 1.99 ($p = 0.48$), suggesting no evidence of serial autocorrelation in the residuals.

Furthermore, Pearson's correlation coefficient of 0.70 indicates a moderately strong positive relationship between the variables. The mean absolute error (MAE) of 1.48, which is lower than the standard error of the estimates (1.94), further supports the accuracy of the estimates.

We evaluated the individual contributions of *VCep*, P_{aut}, and ENSO indicators to the *CDI* by analysing their *p*-values. Among them, the autumn precipitation amount (P_{aut}) has the highest *p*-value at 0.03. This justifies including all variables in the *CDI* equation. Next, the *CDI* time-series for the period 2023–2060 was processed and incorporated into the PARMAX (TVAR)-CSD framework (detailed in Supplementary Methods 2).

As a periodical model, the PARMAX(TVAR)-CSD framework incorporates a cycle parameter (*m*). Figure 5b illustrates the anticipated frequency spectrum for the fitted model parameters based on the AMESEI data (listed in Supplementary Data 1). The red boxes highlight the main cycles ranging from a frequency of 0.05 to 0.10. Based on this analysis, we set the cycle to approximately the peak frequency of 0.06, corresponding to a period *m* of about 41 years. This choice of a 41 year cycle is consistent with the peak frequency identified in the spectral analysis, and is further supported by the validation results, which show that this cycle improves the model's predictive accuracy and aligns with observed patterns in the AMESEI data.

Decadal prediction skill and validation

The effectiveness of any prediction technique hinges on two key attributes: its accuracy and reliability. Determining this requires rigorous validation to avoid potential pitfalls like overfitting, where the model prioritises memorising specific data points over capturing broader patterns. In the context of DDSMs, one crucial step involves partitioning the data into training and validation sets. Striking the balance between these subsets is essential. Overweighting the training set can lead to overtraining, while an inadequate training set can hinder proper learning. The absence of established ratios for training, validation and prediction datasets[26,55] presents a relevant challenge

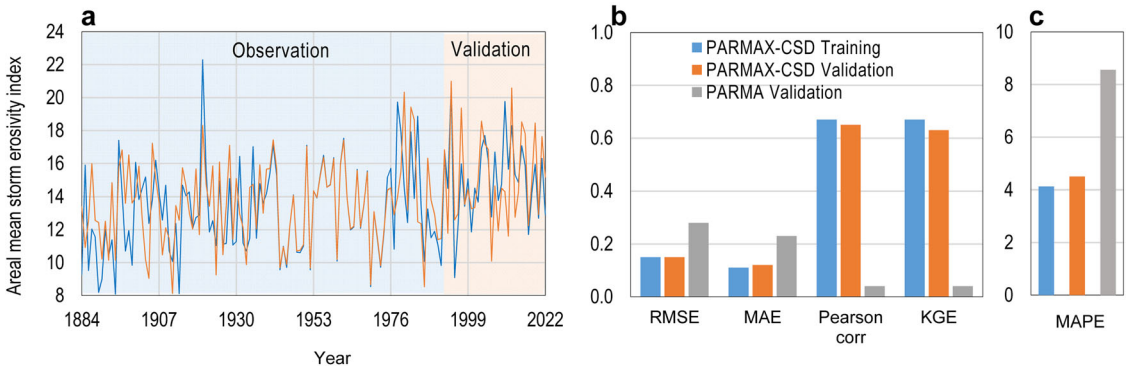

Fig. 6 | Time-series and performance indicators of annual AMESEI in the Mediterranean region. a Comparison of observed (blue line) and modelled (orange line) values, both showing a significant increasing trend (Mann-Kendal test: observed, $p < 0.01$; modelled, $p = 0.02$); (**b**, **c**). Performance indicators (RMSE, MAE, Pearson's correlation coefficient, KGE and MAPE) for training and validation datasets, evaluated with (PARMAX-CSD) and without (PARMA) exogenous input.

Table 1 | Performance comparison of PARMAX(TVAR)-CSD and PARMA(TVAR) models for the Mediterranean region

Statistics	PARMAX(TVAR)-CSD Model		PARMA(TVAR) Model
	Training period (1884–1992)	Validation period (1993–2022)	Validation period (1993–2022)
RMSE (mm day^{-1})	0.15	0.15	0.28
MAE (mm day^{-1})	0.11	0.12	0.23
MAPE (%)	4.12	4.50	8.56
Log Loss	−1.52	−0.04	3.51
r	0.67	0.65	0.04
KGE	0.67	0.63	0.04

RMSE: root mean square error (optimal, 0; worst: +∞); MAE: mean absolute error (optimal, 0; worst: +∞); MAPE: mean absolute percentage error (optimal, 0; worst: +∞); r=Pearson's correlation coefficient (optimum, +1; worst: -1); KGE: Kling-Gupta Efficiency index (worst, -∞ to 1, optimum). Log Loss: logarithmic loss (optimum, 0; worst: +∞). The Log Loss function is used as an uncertainty metric. There are no commonly agreed criteria for establishing what constitutes an acceptable Log Loss value.

in optimising the validation of forecasting techniques. In general, the training dataset should account for a large portion, often >50% of the whole dataset[56]. In this work, the AMESEI dataset was divided into three subsets: training, validation and test. The proportions used were 62%, 17% and 21%, respectively. In our case, the test dataset corresponds to the prediction performed for AMESEI in years 2023- 2060.While there is no fixed rule for the lengths of these datasets, we allocated a 30 year period to the validation dataset to ensure it covered a conventional climate period. This left 109 years for training, which is ~62% of the total dataset. Although this extensive training period provides a robust foundation for the model, the potential for overfitting was carefully mitigated. First, as shown in Fig. 6a, the close agreement between the observed (blue) and modelled (orange) lines during the validation period indicates that the model accurately captures long-term trends without overfitting to training data. Then, the model's performance was assessed using both training and validation subsets, and its error statistics (e.g., RMSE, MAE, MAPE) indicated consistently high accuracy and generalisability across these periods (Table 1), as further illustrated in Fig. 6b, c. For example, the MAPE for the validation period remained below 5%, well within acceptable thresholds[57], with small error values (RMSE, MAE ≤ 0.15), and r and KGE values above 0.5, all indicating satisfactory performance.

We also compared the validation performance of the PARMAX (TVAR)-CSD model (which includes exogenous inputs) with a simpler PARMA(TVAR) model (which does not include exogenous inputs). As shown in Table 1, the PARMAX(TVAR)-CSD model was approximately twice as accurate as the PARMAX(TVAR), with lower RMSE, MAE and MAPE values. Its superior Pearson's correlation coefficient (r) and Kling-Gupta Efficiency (KGE) confirm the benefits of using the longer training dataset alongside exogenous predictors. For the PARMAX(TVAR)-CSD model, Log Loss values of -1.52 (training) and -0.04 (validation) suggest a robust ability to generalise across both datasets, with minimal overfitting. In contrast, the significantly higher Log Loss value of 3.51 for the simpler PARMA(TVAR) model (validation) indicates a much greater uncertainty in its predictions. These results further highlight the advantage of including exogenous variables and the carefully designed dataset partitioning. While the results strongly support the robustness of the PARMAX(TVAR)-CSD model, caution is advised when extending forecasts to decadal scales due to inherent uncertainties.

Storm erosivity index decadal forecast

Understanding and forecasting the complexities of AMESEI dynamics requires navigating a variety of time scales, reflecting the intricate interplay of meteorological and climatic processes. These scales encompass both fleeting short-term changes and overarching long-term trends, posing relevant challenge for comprehending and managing the DHE framework. The last decade has witnessed the Mediterranean region endure numerous DHEs. Clusters of severe thunderstorms unleashed floods and flash floods across central Europe[58]. As Fig. 7 illustrates (blue line), the period between 2009 and 2012 saw storm power exceeding critical thresholds in the region. While accurately predicting the future impacts of climate change on the Mediterranean remains elusive, the increasing trend of storm damage is undeniable. This escalading damage highlights the influence of climate change on the severity and geographical distribution of meteorological phenomena linked to AMESEI.

Building on the robust performance of our model, we have deliberately extended the forecasting horizon beyond the duration of the validation period, which spanned 30 years. Consequently, we extended the length of the forecasting period to 38 years. This extension allowed us to gain insights into potential climate conditions for the full decade 2050–2060. Figure 7 charts the projected annual AMESEI values (orange line) from 2023–2060. While an initial period of relative calm prevails, by 2040 extreme AMESEI values are projected to escalade markedly, exceeding the long-term median (horizontal grey line) by a noteworthy margin. The index then enters a phase of oscillation, fluctuating around the median and mirroring the smoothed trend depicted by the 5 year Gaussian filter erosivity index (dark line).

Following the projected surge in AMESEI by 2040, Fig. 7 indicates a shift in dynamics. The index is expected to stabilise around the long-term median (horizontal bold grey line), oscillating between the boundaries established by the quiet storm limit (bold ochre line). While peaks may still reach the storm erosivity exceedance threshold (bold red line), these events should become less frequent compared to the pre-2040 period. The 5 year

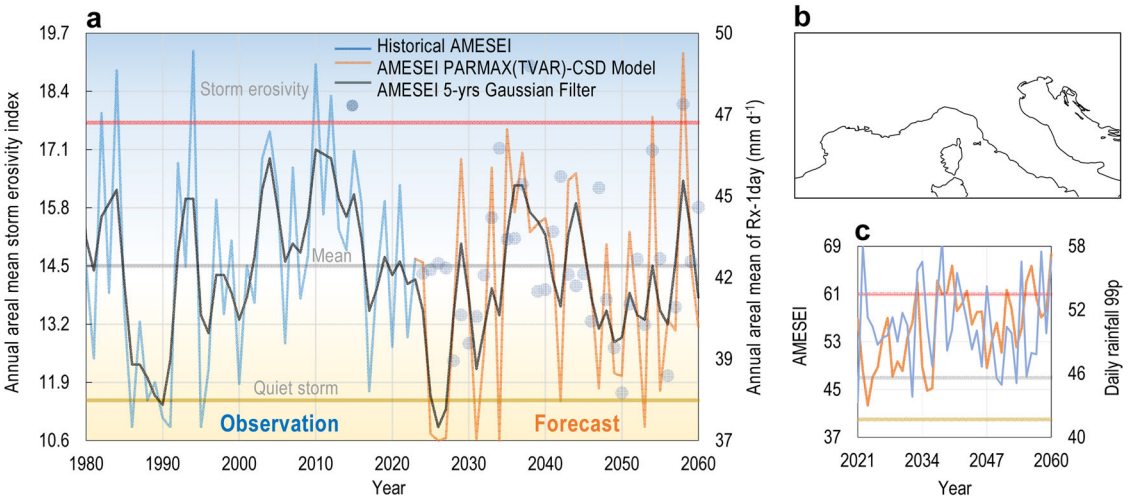

Fig. 7 | Decadal prediction of the storm erosivity index using the PARMAX(T-VAR)-CSD model. a Temporal evolution of observed (1997−2022, blue line) and forecasted (2023−2060, orange line) AMESEI values, with a 5 year Gaussian filter (dark line). Light blue dots represent the annual areal mean of daily rainfall at the 99th percentile (data source: CMIP5 ACCESS1-0 RCP4.5 dataset, Canadian Centre for Climate Modelling and Analysis; http://climexp.knmi.nl); (**b**) Smaller spatial-scale experiment with the PARMAX(TVAR)-CSD model; (**c**). Coevolution of AMESEI (orange line) and the annual areal mean of daily rainfall at the 99th percentile (blue line) showing the mean (bold horizontal grey line), and the 15th (yellow line, quiet storm) and 90th (orange line, storm erosivity exceedance) percentiles.

Gaussian filter erosivity index (dark line) suggests a similar trend. Initially, it is predicted to decrease (dark line), reflecting the stabilisation of AMESEI. Around 2050, some years might even experience low storm erosivity levels (orange line), meaning a return to calmer conditions. However, these periods of reduced activity are unlikely to match the initial tranquillity observed before 2040. The quiet storm limit (15th percentile, bold ochre line) and storm erosivity exceedance threshold (90th percentile, bold red line) were assessed based on the historical distribution of AMESEI values from the baseline period (1997–2022). By defining thresholds associated with variability and extremes, these percentiles capture the lower and upper bounds of typical storm erosivity conditions and provide benchmarks to distinguish between relatively calm periods and extreme storm erosivity events.

The projected AMESEI values (Fig. 7a, orange line) exhibit consistently high interannual variability throughout the forecast period, mirroring the pattern observed in the historical data. While a statistically non-significant linear increase is detected based on the Mann-Kendall test ($p > 0.05$), further investigation is warranted to understand the underlying drivers of this trend.

Figure 7a reveals a compelling comparison between the projected changes in the 5 year Gaussian filter AMESEI (dark line) and the findings from the CMIP5 ACCESS1-0 historical r2i1p1 model output (blue light dots). Notably, the observed projections of the AMESEI filter closely resemble the annual mean of daily rainfall at the 99th percentile forecast under the RCP4.5 emission trajectories. This suggests a potential link between future AMESEI trends and extreme rainfall events as predicted by Global Circulation models (GCMs).

In particular, an interdecadal agreement is advisable for the projected changes over the whole period between two variables (Pearson's correlation coefficient $r = 0.41$). On an interannual scale, however, the agreement between the two forecasts is less pronounced. This could indicate that the previous research on understanding extreme precipitation variability and its usefulness in supporting the decadal prediction of storm erosivity is incomplete.

It has also been shown that such variability, and to a lesser extent the annual ENSO signal, influence heavy precipitation in the Mediterranean. A trend toward greater driving of severe precipitation leading to rainfall erosivity has been observed since the early twentieth century[59] and will likely continue in the future[60,61]. In this respect[61], using a COSMO-Climate-limited area model (COSMO-CLM[62]) that takes into account the complex topography of Mediterranean areas, projected a climate signal for driving erosivity for maximum daily precipitation (Rx-1day), indicating an increase in some regions, particularly in northern Italy. More recently, using a large ensemble of Convection Permitting-Regional Climate Models under the RCP8.5 scenario[63], identify a robust multi-model agreement for an increased frequency of heavy precipitation from central Italy to the northern Balkans, combined with a substantial extension of affected areas and an increase in intensity, area, volume and severity over the French Mediterranean, for the 21st mid-century. Most importantly[64], confirmed that these events are likely to become more intense, more severe and more frequent, with the most dramatic changes expected in the central Mediterranean.

Moving from large to smaller spatial scales (Fig. 7b), it is striking to observe a significant agreement between these latest generation models and the outcomes of the PARMAX(TVAR)-CSD model run. In fact, looking at the projections for this area of the Mediterranean (Fig. 7c), the storm erosivity timeline between 2023 and 2060 increases (orange line), with a significant linear trend (Mann-Kendall trend test). Comparing the ACCESS1-0 model extreme CMIP5 projections (blue line) with the PARMAX(T-VAR)-CSD projections (orange line), the latter shows a much stronger intensification of extreme AMESEI. In particular, the AMESEI increases linearly by 5 mm^2 d^{-1} per decade. Furthermore, the AMESEI values are above the long-term mean (Fig. 7c, grey horizontal line) throughout the forecast period and also reach the 90th percentile around 2040 and before the end of the prediction period. This was also found in the results of [65], which indicate an increase in larger convective storms (mesoscale convective systems), which in turn can lead to larger damaging hydrological events with up to peak precipitation intensities across Europe. Furthermore, the AMESEI enhanced with a 10 year return period (statistically significant Mann-Kendal test, Fig. 8a, orange line) reflects a focus on intermediate extreme events that are more frequent and thus highly relevant for assessing storm erosivity trends over decadal timescales. This return period was selected because it balances the need for capturing impactful events without being skewed by rare outliers. Using a 10 year return period ensures that the projections remain robust and interpretable, especially when linking storm erosivity to other climate indicators, such as flood recurrence or extreme rainfall outcomes. Although higher return periods could represent rarer, more extreme events, these are less relevant to this study's objective of understanding trends in moderately severe events that are likely to shape long-term erosion processes. This is consistent with the growth of areas affected by positive changes in flood recurrence of the CMIP5(E-HYPE-catch) ensemble mean (Fig. 8b, c), increases in extreme rainfall[64], and their

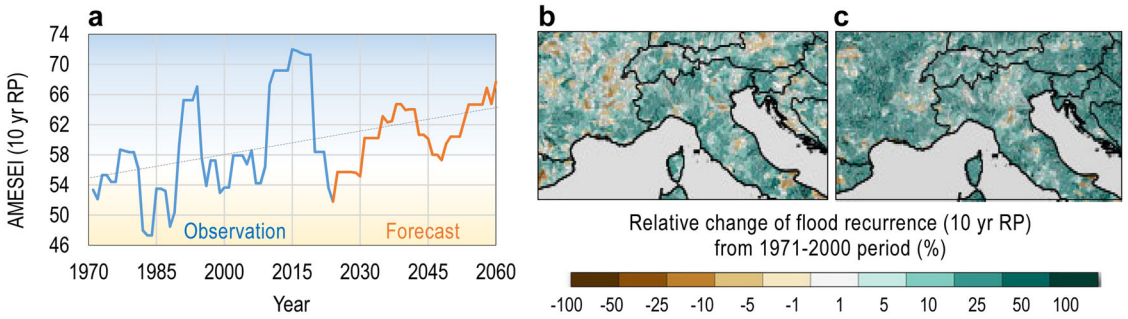

Fig. 8 | Change in hydrological extreme events with 10 year return period. **a** Observed (blue line) and PARMAX(TVAR)-CSD forecasted (orange line) storm index; (**b**). Relative change in flood recurrence (%) from 1971−2000 period as forecasted for (**b**). 2011−2040 and (**c**). 2040−2071 with the CMIP5(E-HYPEcatch) ensemble mean (maps arranged using Climate Explorer; http://climexp.knmi.nl).

erosivity outcomes as predicted by more recent convection-permitting models[27].

According to Panagos et al.[17] and Uber et al.[27], future climate change is projected to have a greater impact on rainfall intensity and erosivity, particularly in Europe. The influence of these hydrological drivers on soil erosion will be increased or decreased depending on the ability of land features, such as soil physical properties, land cover and land use, to buffer their effects under future climatic conditions[66].

Disadvantages and limitations in decadal predictions

The current research shows that computationally efficient, data-driven statistical models can overcome many of the limitations of dynamical models. Our model does not explicitly account for the effects of atmospheric forcing (e.g. CO_2 and aerosol concentrations), but their effects are likely to be implicitly included through the trend components of various variables. Extrapolation of trends may be appropriate when predicting lead times within a decade[1]. However, a comparison with the current convective-permitting dynamical models suggests that they may also be applicable beyond this timeframe.

The scarcity and inhomogeneity of observational data also make it difficult to assess how heavy precipitation varies with climate, even when precipitation observations are aggregated over large areas. Reanalysis data can overcome this issue. In any case, because of the inherent complexity of most real-world variables, it is virtually impossible to predict their future values routinely[67]. Forecast evaluation thus requires a thorough review of potential pitfalls and inaccuracies. Even if a model is well-designed with low bias and variance, the presence of interdependencies between temporally close values can lead to an increase in prediction errors over the forecast horizon[67].

In addition, external climatic factors can cause discrepancies in the model and contribute to new sources of inaccuracy. The anticipated strengthening of the hydrological cycle, resulting in more precipitable water due to the Clausius–Clapeyron relation[68], leads to an increase in sub-daily extreme convective precipitation[69], which complicates forecast accuracy. In particular, extreme rainfall events are strongly influenced by dynamical factors involving feedback from latent heat exchange[70]. These factors are model-dependent and can increase model uncertainty in extreme precipitation responses[33]. It is thus crucial to recognise and overcome these challenges to ensure model robustness and reliability. Future research should prioritise the refinement of data-driven models, while comparing various types of models.

Conclusions

This study highlights the significance of advanced statistical technologies, such as time-varying autoregressive modelling with input climatic information, in enhancing our understanding and prediction capabilities of extreme weather events, specifically in the Mediterranean region. Despite challenges in generating sub-daily rainfall data, our findings underscore the value of these methodologies in addressing the complexities of hydrological extreme time series. While our research demonstrates progress in decadal prediction, it also emphasises the need for uncertainty-aware design paradigms to account for the complexities of predicting future storm-power and hydrological events. Integrating predictive information from dynamical models and statistical approaches could offer promising avenues for enhancing prediction skills and addressing long-term uncertainties[71,72]. By elucidating the implications of extreme weather events on various sectors, including human health and ecosystems, our study underscores the urgent need for improved prediction and understanding to mitigate their adverse effects on society and the environment. Our findings contribute valuable insights to the broader discussion on climate change adaptation and resilience strategies, particularly in regions vulnerable to extreme weather events like the Mediterranean. Continued research efforts in this field are essential for refining prediction models, developing robust adaptation strategies, and fostering resilience in the face of ongoing climate challenges, ultimately contributing to global efforts to address the impacts of extreme weather events.

Data and Methods

We compiled a consistent dataset spanning 1884-2022, incorporating multiple sources to ensure comprehensive coverage and reliability. Key variables include:

- Simple Daily Intensity Index (SDII) and Daily Maximum Rainfall in summer-autumn (Rx1day-sa): Extracted from NOAA/CIRES/DOE 20th Century Reanalysis V3 dataset[73], which provides global atmospheric and surface conditions reconstructed from historical observations;
- Autumn precipitation (P_{aut}): Derived from the GPCC v2020 dataset[74], known for its high-resolution gridded precipitation analysis using station-based data;
- ENSO (Niño3.4): Taken from ERSST v5 dataset[75], offering global sea-surface temperature reconstructions critical for climate variability analysis;
- Correlation map data: Sourced from GLDAS[47,76], which provides a global dataset integrating observation-based meteorological data with model simulations.

For the AMESEI assessment, we opted to rely on reanalysis datasets due to the absence of long-term, high-quality daily precipitation records with complete geographic coverage across Europe. This limitation, highlighted by[77], contributes to ongoing uncertainties in understanding variability in daily heavy precipitation intensities. The selected datasets provide a robust foundation for capturing spatial and temporal trends essential to our analysis.

Predictions were generated using the Time Series Lab[78], Score Edition software V. 1.5 (https://timeserieslab.com), supported by Visual Recurrence Analysis (https://visual-recurrence-analysis.software.informer.com/4.9),

and STATGRAPHICS (http://www.statpoint.net). SELFIS self-similarity analysis software (http://alumni.cs.ucr.edu/~tkarag/Selfis/Selfis.html) and CurveExpert Professional 1.6 (https://www.curveexpert.net) were also used for further statistical and graphical analysis. Model performance was assessed using several criteria, including root mean square error (RMSE), mean absolute error (MAE), mean absolute percentage error (MAPE), Pearson's correlation coefficient (r), and Kling-Gupta efficiency (KGE). Lower values of RMSE, MAE, and MAPE indicate better model performance, with 0 being optimal and infinity representing the worst case. Pearson's correlation coefficient (r) ranges from -1 to +1, with +1 indicating perfect correlation. The Kling-Gupta Efficiency (KGR), which ranges from -∞ to 1 (with 1 being optimal), was used[79] to address the limitations of the commonly used Nash-Sutcliffe efficiency index by ref. 80. It is defined as: $\mathrm{KGE} = 1 - \sqrt{(r-1)^2 + (\alpha-1)^2 + (\beta-1)^2}$. In this equation, r is the linear correlation between observations and simulations, $\alpha = \sigma_s/\sigma_o$ is a measure of the variability of the prediction errors, and $\beta = \mu_s/\mu_o$ is a bias term, where μ and σ are the mean and standard deviation of the observations (sub-script O) and simulations (sub-script S). A KGE value >-0.41 is considered to indicate reasonable model performance. In addition, logarithmic loss (Log Loss) serves as an uncertainty metric, with lower values indicating better model performance and positive infinity representing the worst-case scenario (with no universally accepted thresholds for acceptable values).

Areal mean storm erosivity index assessment

The erosive power of a storm is accounted for by the rainfall erosivity factor (R-factor), which combines the effects of rainfall duration, intensity, and magnitude. To project the effectiveness of damaging hydrological events, it may be advisable to use a simplified form of rainfall erosivity timeframes[81]. Following the RUSLE (Revised Universal Soil Loss Equation) R-factor, which multiplies the kinetic energy of the rainfall (E) by its maximum 30 min intensity (I_{30})[82], we define the Areal Mean Storm Erosivity Index (AMESEI) as the product of rainfall intensity and the highest daily rainfall. In this study, precipitation extremes are defined based on the highest daily rainfall (Rx1day) observed in the summer-autumn period, as this is a key indicator of storm erosivity in the Mediterranean region. Rather than focusing on entire storm events, we use the maximum rainfall intensity over a 24 hour period to quantify precipitation extremes.

The AMESEI ($mm^2\ d^{-1}$) is calculated by multiplying the annual simple daily intensity index (*SDII*), which represents the mean intensity of daily precipitation events over the year, with the highest daily rainfall (Rx1day) in the summer-autumn period, as given in the equation:

$$AMESEI = SDII \cdot Rx1day_{s-aut} \quad (1)$$

Here *SDII* is the annual simple daily intensity index ($mm\ d^{-1}$), and *Rx1day*(*s-aut*) is the highest daily rainfall in summer-autumn ($mm\ d^{-1}$). Based on the equation of[83], *Rx1day*(*s-aut*) expresses the maximum power of landscape disturbance since it covers a high ratio of hourly rainfall maxima for the Mediterranean region. While this approach does not explicitly consider characteristics such as event duration, multiple peaks, or time separation between events (which could be explored in future work), the high correlation between *Rx1day(s-aut)* and extreme rainfall in the Mediterranean supports its use as a reliable proxy for storm erosivity.

Exploratory AMESEI-data analysis and predictability

Exploratory data analysis (EDA) is an agile data analysis technique that focuses on graphical representation of data rather than statistical processing. The current framework includes a collection of data showing AMESEI at various timescales, emphasising its evolutionary aspects such as periodicity and autocorrelations. This can be used as a template to introduce the information for the selection criteria of the initial model. The process of exploring the data starts with basic data plots that evaluate patterns of fluctuation, changes in mean and variance, and the presence of any heteroskedasticity necessary to establish stationary conditions.

Figure 9a shows the annual evolution of AMESEI. The Mann-Kendall test, represented by the grey dashed linear trend, indicates a significant upward trend ($p < 0.01$). The log-transformed AMESEI data are shown in Fig. 9b (purple line), together with its variance evolution (Fig. 9c, green line), which reveals an oscillating trend, but without a significant (Mann-Kendall test, $p > 0.05$) long-term linear trend. In Fig. 9c, the variance of log-transformed AMESEI data is calculated using an 11 year moving window. The choice of an 11 year window aligns with common practices in climate and hydrological studies, where decadal-scale patterns are often analyzed to capture natural variability while smoothing out shorter-term fluctuations. This approach strikes a balance between retaining sufficient temporal resolution and reducing noise, enabling clearer identification of longer-term trends or oscillations. The 11-year period is particularly useful in regions like the Mediterranean, where interannual variability driven by climatic phenomena, such as ENSO, may influence storm erosivity. Future studies could explore different time window lengths to assess the sensitivity of variance trends to the chosen period.

Exploratory data analysis includes autocorrelation function (ACF) and partial autocorrelation function (PACF), which can be used to analyse the correlation of data in time-series. Figure 10a shows the ACF, which connects log-transformed AMESEI data for various lags over residual values. The time-lag (k) shows the correlation between the log-transformed AMESEI data at time *t* and time t + k, which helps to define the order of the autoregressive model required for best data fitting. As the ACF and PACF generated on the standardised residuals of the original AMESEI time series were uncorrelated, we preferred to work on log-transformed data. It has been observed that log transformation leads to a stabilisation of the variance over time and facilitates the assumption of normality[84]. Instead, Fig. 10b shows the PACF, which correlates the log-transformed AMESEI data at different lags, but regresses the time-series values at all shorter lags. In this way, the ACF (Fig. 10a) shows a statistically significant positive correlation at lags 2, 3 and 5, with an abrupt transition to negative correlation, successively. The PACF (Fig. 10b) follows the same pattern, although the time

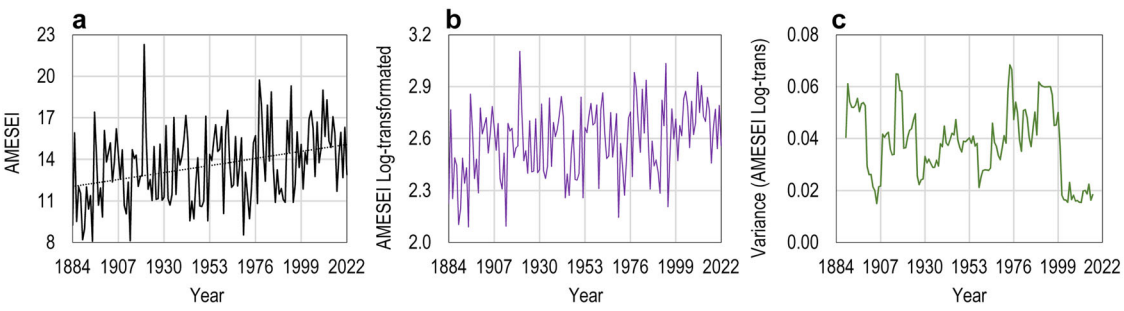

Fig. 9 | Time-series evaluation of the areal mean storm erosivity index for the Mediterranean region (1884−2022). a Annual AMESEI time series (black line), with long-term linear trend (dashed grey line); (**b**). Log-transformed AMESEI data (purple line); (**c**). Variance estimates of log-transformed AMESEI data calculated using an 11 year moving window.

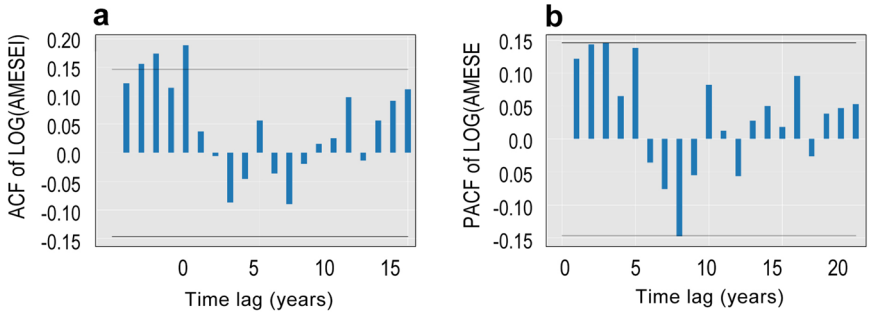

Fig. 10 | Autocorrelation analysis of the areal mean storm erosivity index (AMESEI) for the Mediterranean region (1884−2022). **a** Autocorrelation function (ACF) of log-transformed data, and (**b**). Partial autocorrelation function (PACF) on log-transformed data. Horizontal black lines indicate the 95% confidence limits.

series results are not significantly correlated. According to[85], the model is an ARMA(*P*,*Q*), since the shapes of ACF and PACF follow a similar trend.

The choice to use an autoregressive model of order AR(2) in Eq. 2 was based on the results presented in Fig. 10. Specifically, the ACF (Fig. 10a) showed significant positive correlations at lags 2, 3, and 5, with an abrupt transition to negative correlation afterward. Similarly, the PACF (Fig. 10b) showed a similar trend, with significant correlations at lags 1 and 2, and no significant correlations at higher lags. These results suggest that the AMESEI time series exhibits a significant dependency on its past values at lags 1 and 2, justifying the selection of AR(2) as the appropriate model order. This choice ensures that the model captures the temporal dependencies effectively, without overfitting to higher-order correlations that are not present in the data.

The choice to use the log-transformation proved to be the most appropriate option, as it improved the model performance during both the training and validation phases. The AMESEI residual distribution (not shown) was examined using the McLeod-Li (LM) test[86]. The test results showed that LM has a *p*-value of 0.87, well above the critical threshold of 0.05, indicating that the time series is not-heteroskedastic. Consequently, the preferred model was revised to PARMAX(2,0)*m*-CSD, where $m = 41$ represents the cycle associated with the *location* component. The value of *m* was determined through spectral density analysis, which identifies dominant periodicities in the data by analysing the frequency spectrum of the time series. This approach highlighted a relevant cycle corresponding to a period of ~41 years, which aligns with known decadal to multi-decadal long-term climatic oscillations linked to ocean-atmosphere interactions that influence the Mediterranean region[87–89]. The validity of $m = 41$ was further verified during the validation stage, where its inclusion improved predictive accuracy and supported other model parameters. This systematic assessment ensures that the chosen cycle is both statistically justified and climatologically meaningful.

Finally, predictability was explored in detail using the Hurst (H) exponent, which measures the long-term memory of time series data[90]. In other words, this statistic is crucial for characterising the memory and structural ramification of the time series. In a time series, the exponent defines the rate of stochastic processes, where $0 < H < 1$. The exponent is closely related to the fractal dimension (D) of the time series through the relationship $D = 2–H$. This relationship indicates the autocorrelation or long-term memory characteristics of the time series. A time series with long-term oscillations between high and low values in adjacent pairs is represented by a value <0.5. This suggests a tendency to oscillate across a power-law function, and between high and low values over time. Short-term memory is represented by $H = 0.5$, where (absolute) autocorrelations fall rapidly to zero. A time series with long-term positive memory is indicated by a value of $H > 0.5$, which means that the autocorrelation decreases more slowly than exponentially and according to a power law.

To assess the presence of long-term memory in the AMESEI time series and its potential for forecasting, we employed the Rescaled Range (R/S) analysis, a non-parametric method for estimating the exponent H[91]. The original AMESEI data yielded an H of 0.63, indicative of strong persistence, suggesting that past trends are likely to continue. This supports the potential for reliable forecasting. To investigate the impact of detrending, we recalculated H on the detrended, log-transformed data. The resulting H of 0.51, while still suggesting weak persistence, may be an underestimate due to detrending's potential to distort the true memory properties of the time series by removing trend while leaving other statistical properties unchanged (e.g. [92]).

Model development

Parameterisation of the PARMAX(TVAR)-CSD model. Models can combine the efforts of multiple research teams to produce useful practical results that efficiently build knowledge[93]. In particular, given how these effects evolve over time, predictive models can reflect the influence of modest steps across multiple domains[93]. The main advantages of using the PARMAX(TVAR)-CSD model emerge when dealing with the largest amounts of information exchanged between states at time *t*–1 and time *t*, with the help of exogenous input climatic forcing, for decadal time in advance.

The random variable *y* at time *t* (y_t) is represented as depending on both y_{t-i} and a fixed period m in the initial phase. A unique strategy for adding the periodic (*m*) component in the autoregressive model uses an additive structure consisting of two components.

The first is considered to be the *location* component[94]:

$$y_t = S_{t-i}(\mathrm{AR}) + m_{t-jm} \tag{2}$$

where y_t is the AMESEI time series to be projected at time t over the year with period *m*; S_t is the random component, characterized as an AR (autoregressive) process with a m_t (deterministic) periodic cycle of time *m*. The relevant parameters for the location component are outlined below:

$$\mu(L) = \mathrm{Level_L} + \mathrm{AR}(2) + \mathrm{Periodical}(41) + X \cdot \beta L + \mathrm{Score}(1)_\mathrm{L} \tag{3}$$

where μ(L) is the model averaging; AR(2) is the autoregressive component of order 2. This suggests that the model depends on its past values y_{t-i}, where $i = 1$ or 2. X is the exogenous variable, while β_L is the corresponding parameter. The final score factor is the score vector of the (predictive) density of the observed time series, which is determined by the ability of score-driven models to deviate from the normal distribution.

The score-driven model has three main advantages[78]: (i) the filtered estimates of the time-varying parameter are optimal in a Kullback-Leibler, that is, an appropriate filtering mechanism over the genuine data generation process; (ii) because the models are observation-driven, their probability has been identified in closed form; and (iii) these models have comparable predictive performance to their parameter-driven competitors[95].

The parameter equation of the second *log-scale* component is as follows:

$$\sigma(S) = \exp\left(\mathrm{Level_S} + \mathrm{X} \cdot \beta_S + \mathrm{Score}(1)_\mathrm{S}\right) \tag{4}$$

σ denotes the standard deviation. β_S is the corresponding parameter. As the time series is not heteroskedastic, the log-scale component, Eq. (4), has no autoregressive (AR) factor. In Eqs. (3) and (4), $Level_L$ and $Level_S$ represent the baseline or constant components for the location and scale (log-scale) components of the model, respectively. LevelL in Eq. (3) captures the overall mean or trend in the location component of the autoregressive model. It is a constant that adjusts the model to fit the baseline level of the time series before considering the autoregressive and periodic components. LevelS in Eq. (4) acts as the baseline level for the log-scale component, which is primarily used for modelling the variance or volatility in the data. It ensures that the logarithmic transformation of the variance has a meaningful baseline around which fluctuations can occur. These terms are essential for setting the baseline levels of the two components and ensuring that the model can account for both the trend (location) and the fluctuations (scale) in the time series data[96] and[40] provide further insights and numerical solutions to Eq. (2), (3) and (4).

Model design with exogenous climatic input

We employed an exogenous climatic input to establish and predict AMESEI for the coming decades, using the PARMAX(TVAR)-CSD model. This model was chosen for its ability to represent some of the internal natural variability involved in AMESEI, while also responding to climatic constraints. A Climate Driving Index (*CDI*) was used to enhance the data model. The inclusion of *CDI* features in the PARMAX(TVAR)-CSD model helps to accurately capture the behaviour of an autoregressive time series. The *CDI* is a composite index that incorporates multiple climatic variables known to influence storm erosivity. In particular, the variable *X* in Eq. (5) must include the *CDI*, which is a combination of the El Niño Southern Oscillation (ENSO(3.4)), autumn precipitation (P_{aut}, mm d^{-1}) and the variation coefficient of extreme precipitation (*VCep*). The *CDI* is then defined as a function of these variables according to the following expression:

$$CDI = \left(10 + ENSO(3.4) + P_{aut}\right) \cdot \left(1 + \frac{SD(SDII_{ann} - Rx(1\mathrm{d}))_{sum-aut}}{M(SDII_{ann} - Rx(1\mathrm{d}))_{sum-aut}}\right) \quad (5)$$

where *SD* and *M* represent the standard deviation and mean, respectively, calculated over extreme rainfall ($SDII_{ann}$ and $Rx1d_{summ\text{-}aut}$) in mm d^{-1}. The form of this equation was developed based on an integration of known climate drivers and their relationship to storm erosivity. The rationale for the combination of these specific variables lies in their established roles in influencing precipitation patterns and storm intensity. Specifically, ENSO is known to affect seasonal rainfall patterns and variability, which can influence the frequency and intensity of extreme weather events[97]. Autumn precipitation (P_{aut}) has been identified as a key factor in determining regional hydrological conditions[98]. The inclusion of the variation coefficient of extreme precipitation (*VCep*) captures the variability of extreme rainfall events, further enhancing the predictive power of the *CDI*. The equation was derived through a combination of empirical relationships observed in the Mediterranean region's climate data and the need to create a comprehensive index that could effectively capture the climatic drivers influencing AMESEI. The *CDI* shows a stronger relationship with AMESEI than when the INDIVIDUAL variables (ENSO, P_{aut} and *VCep*) are considered separately, making it a more robust predictor for future storm erosivity patterns.

Data availability

All data used in this study are freely available. Source AMESEI dataset for graphs and chars is provided in Supplementary Data 1.

Received: 28 March 2024; Accepted: 6 March 2025;
Published online: 18 March 2025

References

1. Sahastrabuddhe, R. & Ghosh, S. Does statistical model perform at par with computationally expensive general circulation model for decadal prediction? *Environ. Res. Lett.***16**, 064028 (2021).
2. Salas, J., Saha, A. & Ravela, S. Learning inter-annual flood loss risk models from historical flood insurance claims. *J. Environ. Manag.***347**, 118862 (2023).
3. Schiermeier, Q. The real holes in climate science. *Nature* **463**, 284–287 (2010).
4. Bhatia, U. & Ganguly, A. R. Precipitation extremes and depth-duration-frequency under internal climate variability. *Sci. Rep.* **9**, 9112 (2019).
5. Van der Wiel, K. & Bintanja, R. Contribution of climatic changes in mean and variability to monthly temperature and precipitation extremes. *Commun. Earth Environ.* **2**, 1 (2021).
6. Bird, L. J., Bodeker, G. E. & Clem, K. R. Sensitivity of extreme precipitation to climate change inferred using artificial intelligence shows high spatial variability. *Commun. Earth Environ.* **4**, 469 (2023).
7. Faranda, D. et al. A climate-change attribution retrospective of some impactful weather extremes of 2021. *Weather Clim. Dynam.* **3**, 1311–1340 (2022).
8. Smith, D. M. et al. Robust skill of decadal climate predictions. *npj Clim. Atmos. Sci.* **2**, 13 (2019).
9. Heikkinen, R. K. et al. Fine-grained climate velocities reveal vulnerability of protected areas to climate change. *Sci. Rep.* **10**, 1678 (2020).
10. De Luca, D. L. & Galasso, L. Stationary and non-stationary frameworks for extreme rainfall time series in southern Italy. *Water* **10**, 1477 (2018).
11. Panagos, P. et al. Global rainfall erosivity assessment based on high-temporal resolution rainfall records. *Sci. Rep.* **7**, 4175 (2017).
12. Schmidt, S., Alewell, C., Panagos, P. & Meusburger, K. Regionalization of monthly rainfall erosivity patterns in switzerland. *Hydrol. Earth Syst. Sci.* **20**, 4359–4373 (2016).
13. Reimann, L., Vafeidis, A. T., Brown, S., Hinkel, J. & Tol, R. S. J. Mediterranean UNESCO world heritage at risk from coastal flooding and erosion due to sea-level rise. *Nat. Commun.* **9**, 4161 (2018).
14. Bagwan, W. A. An assessment of rainfall-induced land degradation condition using erosivity density (ED) and heatmap method for Urmodi River watershed of Maharashtra, India. *J. Sediment. Environ.* **5**, 279–292 (2020).
15. Diodato, N., Ljungqvist, F. C. & Bellocchi, G. Fingerprint of climate change in precipitation aggressiveness across the central Mediterranean (Italian) area. *Sci. Rep.* **10**, 22062 (2020).
16. Bezak, N., Borrelli, P. & Panagos, P. Exploring the possible role of satellite-based rainfall data in estimating inter- and intra-annual global rainfall erosivity. *Hydrol. Earth Syst. Sci.* **26**, 1907–1924 (2022).
17. Panagos, P. et al. Global rainfall erosivity projections for 2050 and 2070. *J. Hydrol.* **610**, 127865 (2022).
18. Wang, L. et al. Rainfall erosivity index for monitoring global soil erosion. *CATENA* **234**, 107593 (2024).
19. UNEP/MAP. *Mediterranean Action Plan of the United Nations Environment Programme, Convention for the Protection of the Marine Environment and the Coastal Region of the Mediterranean.* https://www.unep.org/unepmap/resources/factsheets/climate-change (1995).
20. Zittis, G., Hadjinicolaou, P., Klangidou, M., Proestos, Y. & Lelieveld, J. A multi-model, multi-scenario, and multi-domain analysis of regional climate projections for the Mediterranean. *Reg. Environ. Change* **19**, 2621–2635 (2019).
21. Tramblay, Y. et al. Challenges for drought assessment in the Mediterranean region under future climate scenarios. *Earth Sci. Rev.* **210**, 103348 (2020).
22. Benetó, P. & Khodayar, S. On the need for improved knowledge on the regional-to-local precipitation variability in eastern Spain under climate change. *Atmos. Res.* **290**, 106795 (2023).
23. Ghazi, B., Przybylak, R. & Pospieszyńska, A. Projection of climate change impacts on extreme temperature and precipitation in central Poland. *Sci. Rep.* **13**, 18772 (2023).

24. Runge, J. et al. Causal inference for time series. *Nat. Rev. Earth Environ.***4**, 487–505 (2023).
25. Tierney, J. E. et al. Past climates inform our future. *Science.* **370**, eaay3701 (2020).
26. Zhang, X. et al. Complexity in estimating past and future extreme short-duration rainfall. *Nat. Geosci.* **10**, 255–259 (2017).
27. Uber, M., Haller, M., Brendel, C., Hillebrand, G. & Hoffmann, T. Past, present and future rainfall erosivity in central Europe based on convection-permitting climate simulations. *Hydrol. Earth Syst. Sci.* **28**, 87–102 (2024).
28. Müller, S. K. et al. Evaluation of Alpine-Mediterranean precipitation events in convection-permitting regional climate models using a set of tracking algorithms. *Clim. Dyn* **61**, 939–957 (2023).
29. Yoden, S. & Yoshida, K. Impacts of solar activity variations on Climate. In *Solar-Terrestrial Environmental Prediction*, (ed. Kusano, K.) 445–459 (Springer, 2023).
30. Baumberger, C., Knutti, R. & Hirsch Hadorn, G. Building confidence in climate model projections: an analysis of inferences from fit. *WIREs Clim. Change* **8**, e454 (2017).
31. Eyring, V. et al. Taking climate model evaluation to the next level. *Nat. Clim. Change* **9**, 102–110 (2019).
32. Sandgathe, S. et al. Exploring the need for reliable decadal prediction. *Bull. Amer. Meteor. Soc.* **101**, E141–E145 (2020).
33. Zhang, W. et al. Constraining extreme precipitation projections using past precipitation variability. *Nat. Commun.* **13**, 6319 (2022).
34. Diodato, N., Lanfredi, M. & Bellocchi, G. Long-range, time-varying statistical prediction of annual precipitation in a Mediterranean remote site. *Environ. Res. Clim.* **2**, 045011(2023).
35. Meehl, G. A. et al. Initialized Earth system prediction from subseasonal to decadal timescales. *Nat. Rev. Earth Environ.* **2**, 340–357 (2021).
36. Carleton, T. A. & Hsiang, S. M. Social and economic impacts of climate. *Science* **353**, aad9837 (2016).
37. Zhang, Y. et al. Comparison of the ability of ARIMA, WNN and SVM models for drought forecasting in the sanjiang plain, China. *Nat. Resour. Res.* **29**, 1447–1464 (2020).
38. Islam, F. & Imteaz, M. A. Use of teleconnections to predict western Australian seasonal rainfall using ARIMAX model. *Hydrology* **7**, 52 (2020).
39. Diodato, N. & Bellocchi, G. Using historical precipitation patterns to forecast daily extremes of rainfall for the coming decades in Naples (Italy). *Geoscience* **8**, 293 (2018).
40. Lit, R. *Forecasting The VIX In The Midst of COVID-19*. https://timeserieslab.com/articles/rlit_vix.pdf (2020).
41. Schär, S., Marelli, S. & Sudret, B. Emulating the dynamics of complex systems using autoregressive models on manifolds (mNARX). *Mech. Syst. Signal Process.* **208**, 110956 (2024).
42. Bezak, N., Mikoš, M., Borrelli, P., Liakos, L. & Panagos, P. An in-depth statistical analysis of the rainstorms erosivity in Europe. *CATENA* **206**, 105577 (2021).
43. Diodato, N. & Bellocchi, G. MedREM, a rainfall erosivity model for the Mediterranean region. *J. Hydrol.* **387**, 119–127 (2010).
44. Lionello, P. et al. The Mediterranean climate: an overview of the main characteristics and issues. In *Mediterranean climate variability*, (eds. Lionello, P., Malanotte-Rizzoli, P., Boscolo, R.) 1–26 (Amsterdam, Elsevier, 2006).
45. Sun, Y. et al. Feasibility of predicting Vietnam's autumn rainfall regime based on the tree-ring record and decadal variability. *Climate* **6**, 42 (2018).
46. Liu, Y. et al. Enhanced multi-year predictability after El Niño and La Niña events. *Nat. Commun.* **14**, 6387 (2023).
47. Rodell, M. et al. The global land data assimilation system. *Bull. Amer. Meteor. Soc.* **85**, 381–394 (2004).
48. de Benavides-Solorio, J. D. & MacDonald, L. H. Measurement and prediction of post-fire erosion at the hillslope scale, colorado front range. *Int. J. Wildland Fire* **14**, 457–474 (2005).
49. Kraskov, A., Stogbauer, H. & Grassberger, P. Estimating mutual information. *Phys. Rev. E* **69**, 066138 (2004).
50. Gao, S., Ver Steeg, G. & Galstyan, A. Efficient estimation of mutual information for strongly dependent variables. *Artif. Intell. Statist.* **38**, 277–286 (2015).
51. Türkeş, M. & Tatlı, H. Use of the spectral clustering to determine coherent precipitation regions in Turkey for the period 1929–2007. *Int. J. Climatol.* **31**, 2055–2067 (2011).
52. Alpert, P. et al. The paradoxical increase of Mediterranean extreme daily rainfall in spite of decrease in total values. *Geophys. Res. Lett.* **29**, 31-1–31-4 (2002).
53. Nerlove, M. & Wallis, K. F. Use of the Durbin-Watson statistic in inappropriate situations. *J. Econom. Soc.* **34**, 235–238 (1966).
54. Hill, R. J. & Flack, H. D. The use of the Durbin–Watson d statistic in rietveld analysis. *J. Appl. Crystallogr.* **20**, 356–361 (1987).
55. Wunsch, A., Liesch, T. & Broda, S. Groundwater level forecasting with artificial neural networks: a comparison of long short-term memory (LSTM), convolutional neural networks (CNNs), and non-linear autoregressive networks with exogenous input (NARX). *Hydrol. Earth Syst. Sci.* **25**, 1671–1687 (2021).
56. Guo, B. et al. Prediction of groundwater level under the influence of groundwater exploitation using a data-driven method with the combination of time series analysis and long short-term memory: a case study of a coastal aquifer in Rizhao City, Northern China. *Front. Environ. Sci.* **11**, 1253949 (2023).
57. Osteragova, E. & Osterag, O. Forecasting using simple exponential smoothing method. *Acta Electrotechni. Informatica.* **12**, 62–66 (2012).
58. Feldmann, M. et al. Hailstorms and rainstorms versus supercells—a regional analysis of convective storm types in the Alpine region. *npj Clim Atmos Sci* **6**, 19 (2023).
59. Fischer, F. K., Winterrath, T. & Auerswald, K. Temporal- and spatial-scale and positional effects on rain erosivity derived from point-scale and contiguous rain data, hydrol. *Earth Syst. Sci.* **22**, 6505–6518 (2018).
60. Fowler, H. J. et al. Anthropogenic intensification of short-duration rainfall extremes. *Nat. Rev. Earth Environ.* **2**, 107–122 (2021).
61. Zollo, A. L., Rillo, V., Bucchignani, E., Montesarchio, M. & Mercogliano, P. Extreme temperature and precipitation events over Italy: assessment of high-resolution simulations with COSMO-CLM and future scenarios. *Int. J. Clim.* **36**, 987–1004 (2016).
62. Rockel, B., Will, A. & Hense, A. The regional climate model COSMO-CLM (CCLM). *Meteorol, Z* **17**, 347–348 (2008).
63. Caillaud, C. et al. Mediterranean heavy precipitation events in a warmer climate: robust versus uncertain changes with a large convection-permitting model ensemble. *Geophys. Res. Lett.* **51**, e2023GL105143 (2023).
64. Müller, S. K. et al. The climate change response of alpine-mediterranean heavy precipitation events. *Clim. Dyn.* **62**, 165–186 (2024).
65. Chan, S. C. et al. Large-scale dynamics moderate impact-relevant changes to organised convective storms. *Commun. Earth Environ.* **4**, 8 (2023).
66. Li, Z. & Fang, H. Impacts of climate change on water erosion: a review. *Earth Sci. Rev.* **163**, 94–117 (2016).
67. Haben, S. Verification and evaluation of load forecast models. In *Core Concepts and Methods in Load Forecasting*. (eds. Haben, S., Voss, M., Holderbaum W.) 89–105 (Springer Cham, 2023).
68. Berg, P., Moseley, C. & Haerter, J. O. Strong increase in convective precipitation in response to higher temperatures. *Nat. Geosci.* **6**, 181–185 (2013).

69. Moustakis, Y., Onof, C. J. & Paschalis, A. Atmospheric convection, dynamics and topography shape the scaling pattern of hourly rainfall extremes with temperature globally. *Commun. Earth Environ.* **1**, 11 (2020).
70. Nie, J. et al. Dynamic amplification of extreme precipitation sensitivity. *Proc. Natl Acad. Sci. USA.* **115**, 9467–9472 (2019).
71. Schlef, K. E., Baptiste, F. & Casey, B. Comparing flood projection approaches across hydro-climatologically diverse United States river Basins. *Water Resour Res*. **57**, e2019WR025861 (2021).
72. Tsartsali, E. E. et al. Predicting precipitation on the decadal timescale: a prototype climate service for the hydropower sector. *Clim. Service***32**, 100422 (2023).
73. Slivinski, L. C. et al. Towards a more reliable historical reanalysis: improvements for version 3 of the twentieth century reanalysis system. *Q J R Meteorol Soc* **145**, 2876–2908 (2019).
74. Schneider, U., Becker, A., Finger, P., Rustemeier, E. & Ziese, M. *GPCC Full Data Monthly Product Version 2020 at 0.25°: Monthly Land-Surface Precipitation from Rain-Gauges built on GTS-based and Historical Data.* https://opendata.dwd.de/climate_environment/GPCC/html/fulldata-monthly_v2020_doi_download.html (2020).
75. Huang, B. et al. Extended reconstructed sea surface temperature version 5 (ERSSTv5), upgrades, validations, and intercomparisons. *J. Climate.* **30**, 8179–8205 (2017).
76. Cornes, R., van der Schrier, G., van den Besselaar, E. J. M. & Jones, P. D. An ensemble version of the E-OBS temperature and precipitation datasets. *J. Geophys. Res. Atmos.* **123**, 9391–9409 (2018).
77. Tabari, H. & Willems, P. Lagged influence of Atlantic and Pacific climate patterns on European extreme precipitation. *Sci Rep* **8**, 5748 (2018).
78. Lit, R., Koopman, S. J. & Harvey, A. C. *Time Series Lab.* https://timeserieslab.com/ (2022).
79. Gupta, H. V., Kling, H., Yilmaz, K. K. & Martinez, G. F. Decomposition of the mean squared error and NSE performance criteria: Implications for improving hydrological modelling. *J. Hydrol.* **377**, 80–91 (2009).
80. Nash, J. E. & Sutcliffe, J. V. River flow forecasting through conceptual models Part I—a discussion of principles. *J.Hydrol.* **10**, 282–290 (1970).
81. Blöschl, G. et al. Changing climate shifts timing of European floods. *Science* **357**, 588–590 (2017).
82. Brown, L. C. & Foster, G. R. Storm erosivity using idealized intensity distributions. *Trans. ASABE.* **30**, 379–386 (1987).
83. Diodato, N. Predicting RUSLE (Revised Universal Soil Loss Equation) monthly erosivity index from readily available rainfall data in Mediterranean area. *Environ.* **25**, 63–70 (2006).
84. Hu, W., Tong, S., Mengersen, K. & Connell, D. Weather variability and the incidence of cryptosporidiosis: comparison of time series poisson regression and SARIMA models. *Annal. Epidemiol.* **17**, 679–688 (2007).
85. Valenzuela, O. et al. Hybridization of intelligent techniques and ARIMA models for time series prediction. *Fuzzy Set Syst.***159**, 821–845 (2008).
86. McLeod, A. I. & Li, W. K. Diagnostic checking ARMA time series models using squared residual autocorrelations. *J. Time Series Anal.* **4**, 269–273 (1983).
87. Knight, J. R., Folland, C. K. & Scaife, A. A. Climate impacts of the Atlantic multidecadal oscillation. *Geophys. Res. Lett.* **33**, L17706 (2006).
88. Sutton, R. T. & Dong, B. Atlantic Ocean influence on a shift in European climate in the 1990s. *Nat. Geosci.* **5**, 788–792 (2012).
89. Mariotti, A., Pan, Y., Zeng, N. & Alessandri, A. Long-term climate change in the Mediterranean region in the midst of decadal variability. *Clim. Dynam.* **44**, 1437–1456 (2015).
90. Hurst, H. E. Long-term storage capacity of reservoirs. *Trans. Am. Soc. Civil Eng.***116**, 770–799 (1951).
91. Mandelbrot, B. B. & Taqqu, M. S. Robust R/S analysis of long run serial correlation. *Bull. Int. Stat. Inst.* **48**, 59–104 (1979).
92. Kantelhardt, J. W. et al. Detecting long-range correlations with detrended fluctuation analysis. *Physica A. Statist. Mech. Appl.* **295**, 441–454 (2001).
93. Mulligan, M. & Wainwright, J. Modelling and model building. In *Environmental Modelling: Finding Simplicity in Complexity* (eds. Wainwright, J. & Mulligan, M.) 494 (Wiley, 2004).
94. Montgomery, D. C., Jennings, C. L., & Kulahci, M. *Introduction to Time Series Analysis and Forecasting*. (John Wiley and Sons, 2008).
95. Koopman, S. J., Lucas, A. & Scharth, M. Predicting time-varying parameters with parameter-driven and observation-driven models. *Rev. Econom. Statist.* **98**, 97–110 (2016).
96. Basawa, I. V., Lun, R. & Shao, Q. First-order seasonal autoregressive processes with periodically varying parameters. *Stat. Probab. Lett.* **67**, 299–306 (2004).
97. Ropelewski, C. F. & Halpert, M. S. Global and regional scale precipitation patterns associated with the El Niño/southern oscillation. *Monthly Weather Rev.* **115**, 1606–1626 (1987).
98. Valero, F. et al. Coupled modes of large-scale climatic variables and regional precipitation in the western Mediterranean in autumn. *Clim. Dynam.* **22**, 307–323 (2004).
99. Panagos, P. et al. Monthly rainfall erosivity: conversion factors for different time resolutions and regional assessments. *Water* **8**, 119 (2016).
100. Gaume, E. et al. Mediterranean extreme floods and flash floods. In *The Mediterranean Region Under Climate Change*. eds. Moatti, J. P. & Thiebault, S. 736 (IRD Éditions, 2018).

Acknowledgements

This research was performed as an investigator-driven study without financial support.

Author contributions

N.D. developed the original research design and collected and analysed the basic precipitation data. N.D., C.D.S., and G.B. wrote the article together and made the interpretations together. All authors reviewed the final manuscript.

Competing interests

The authors declare no competing interests.

Additional information

Supplementary information The online version contains supplementary material available at https://doi.org/10.1038/s43247-025-02196-2.

Correspondence and requests for materials should be addressed to Gianni Bellocchi.

Peer review information *Communications Earth & Environment* thanks the anonymous reviewers for their contribution to the peer review of this work. Primary Handling Editor: Alireza Bahadori. A peer review file is available.